Analysis of nonlinear dynamics on arbitrary geometries with the Virtual Cell

James C. Schaff and Boris M. Slepchenko
Center for Biomedical Imaging Technology, University of Connecticut Health Center, Farmington, Connecticut 06030

Yung-Sze Choi
Department of Mathematics, University of Connecticut, Storrs, Connecticut 06269

John Wagner
Center for Biomedical Imaging Technology, University of Connecticut Health Center, Farmington, Connecticut 06030

Diana Resasco
Department of Computer Science, Yale University, New Haven, Connecticut 06520

Leslie M. Loew
Center for Biomedical Imaging Technology, University of Connecticut Health Center, Farmington, Connecticut 06030

(Received 28 September 2000; accepted for publication 4 January 2001)

The Virtual Cell is a modeling tool that allows biologists and theorists alike to specify and simulate cell-biophysical models on arbitrarily complex geometries. The framework combines an intuitive, front-end graphical user interface that runs in a web browser, sophisticated server-side numerical algorithms, a database for storage of models and simulation results, and flexible visualization capabilities. In this paper, we present an overview of the capabilities of the Virtual Cell, and, for the first time, the detailed mathematical formulation used as the basis for spatial computations. We also present summaries of two rather typical modeling projects, in order to illustrate the principal capabilities of the Virtual Cell. © *2001 American Institute of Physics.* [DOI: 10.1063/1.1350404]

In the 50 plus years since Hodgkin and Huxley's groundbreaking work with the squid giant axon, mathematical modeling has slowly but steadily become a viable approach to studying cell biophysical processes and phenomena. This has undoubtedly resulted from a number of key developments, including advances in quantitative biology, computer science, and mathematics. Of great importance have been the development of techniques leading to the elucidation of the myriad pathways underlying many of the cell's basic functions; the advances in computer hardware and high-performance computing; and more sophisticated analytical and numerical methods for dealing with systems of nonlinear differential equations. Indeed, such advances have given way to more quantitative models involving more detailed descriptions of mechanisms, cellular structure, and geometries. In turn, the more successful models have helped to stimulate the field as a whole, and to introduce modeling techniques into more mainstream biology. Despite this progress, however, cellular modeling remains limited to the more mathematically and/or computationally gifted few. This is especially true with respect to spatial modeling, where the mathematical and computational techniques are much more sophisticated, and the computational requirements much higher; the problem only grows as models incorporate more detailed descriptions of mechanisms, structure, and geometry. Unfortunately, very few tools exist to aide the modeler in treating detailed spatial models on complex three-dimensional geometries. A number of mature packages exist for treating whole-cell models, including Gepasi,[1] and XPPAUT (Bard Ermentrout, XPPAUT 4.5, see http://www.pitt.edu/phase/), as well as spatial tools designed for the unique demands of modeling neuronal systems, including neuron,[2] and genesis.[3] Not one of these tools, however, can treat both nonspatial as well as full three-dimensional spatial models, and those that can treat spatial problems impose rather severe geometric constraints. The Virtual Cell was designed with these problems in mind. Our primary goal is to develop a tool that allows experimental biologists to specify and simulate arbitrarily complex cell-biophysical models on complex geometries, without requiring extensive knowledge about the underlying mathematical and computational techniques. In this paper, we present an overview of the capabilities of the Virtual Cell, as well as the mathematical formulation used as the basis for spatial computations. We then present summaries of two rather typical modeling projects, in order to illustrate the principal capabilities of the Virtual Cell.

I. VIRTUAL CELL OVERVIEW

The Virtual Cell is a computational modeling framework and tool, designed for biologists and theorists alike, for constructing and simulating spatial and nonspatial cell physiological models. Its most important features include an intuitive user interface that runs in a web browser, a back-end database for storing and retrieving physiological models and simulation results, and sophisticated mathematical and computational algorithms. Our approach separates the model

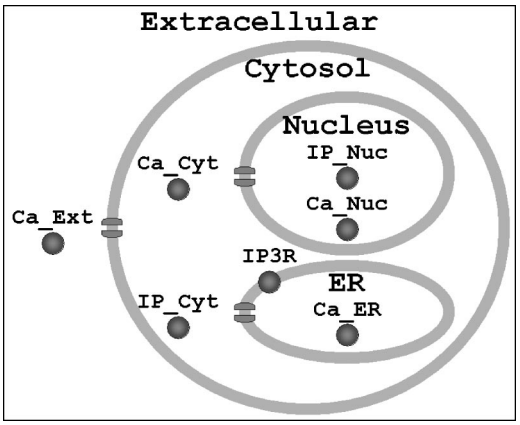

FIG. 1. Typical model compartment layout, showing the tree-like layout of four compartments (Extracellular, Cytosol, ER, and Nucleus) and their enclosing membranes (black circles). Also shown are several species (Ca_Ext, Ca_Cyt, IP3R, IP_Nuc, etc.), and three fluxes (embedded in membranes, not labeled).

from the geometry—this allows the physiological model to be mapped to different user-defined geometries, which can be either whole-cell (''point'') geometries or spatial geometries in one, two or three dimensions. It is not until a simulation is run that the model and geometry are linked together; thus, a simulation can be thought of as a pairing of a physiological model with a geometry, as well as the settings specifying initial and boundary conditions and parameters. The simulations are then run on our cluster of Compaq DS20 computers, and the results are returned to the user for visualization. An export utility can be used to export the data to a range of formats for use in other visualization packages.

A. Physiological models

Conceptually, a physiological model can be thought of as a collection of hypotheses that are assembled in an attempt to understand a physiological phenomenon or process. Operationally, a physiological model consists of a description of the organization of the relevant cellular compartments, molecular and chemical species, chemical reactions among species, and fluxes between cellular compartments. In this light, the hypotheses consist of the selection of compartments, how the compartments are arranged topologically, which species are present, which reactions are involved, the kinetics of the reactions, and so on. The physiological model, therefore, represents a chemical reaction system of species, reactions and fluxes spanning any number of compartments and membranes. Figure 1 illustrates several of the basic model components. The model shown contains four compartments (Extracellular, Cytosol, Nucleus, and ER), three membranes (unlabeled; the gray circles), seven species (Ca_Ext, Ca_Cyt, IP_Cyt, IP3R, IP_Nuc, Ca_Nuc, and Ca_ER), and three fluxes (unlabeled; they are embedded in the membranes). Note that reactions are not shown in this figure.

A compartment represents a cellular structure or organelle that is structurally separated from other compartments via a membrane. These compartments can be contained in a ''parent,'' or enclosing, compartment, yielding a hierarchy of compartments in a treelike structure. In this decomposition of the cell, a compartment may ''communicate'' or interact with its parent and its children, but not with any other compartment in the hierarchy. This intercompartmental communication takes the form of membrane fluxes, typically arising from channels, pumps, and other transport mechanisms in the membrane. In Fig. 1 the compartments are arranged such that Cytosol is contained in Extracellular, and both Nucleus and endoplasmic reticulum (ER) are contained in Cytosol. With this hierarchy, it should be clear that communication between ER and Nucleus is not permitted, while that between ER and Cytosol is.

Species are the molecular or chemical species hypothesized to be involved in the process under investigation. They are assigned to compartments or membranes, and may then participate in reactions and fluxes. Thus, in addition to being used to represent chemical constituents inside compartments and membranes, they are also used, for example, in membranes to represent channels or pumps, often in the form of channel or pump states. Figure 1 also shows two species, calcium and inositol-1,4,5-trisphosphate (IP_3), distributed across the four compartments. Note that while every compartment contains calcium, not all contain IP_3. Within each compartment, the species are given names unique to the compartment.

Species concentrations change due to diffusion, reactions and fluxes. Reactions are chemical reactions occurring between species in a single compartment, or between species in a compartment and species in a related membrane. The latter case is used, for example, to represent the binding of a molecular species with a channel or pump. Fluxes represent inter-compartmental fluxes of a single species, and are therefore limited to membranes. In our representation, fluxes are merely flux functions, though their rate can be controlled by the concentration of other species in the membrane, as well as the compartments the membrane separates. Thus, channels are often represented as both a flux and some number of associated channel state species, all embedded in the membrane; state transitions are then regulated by compartmental and membrane-bound species. Figure 1 shows three fluxes, one each in the plasma membrane, the ER membrane, and the nuclear membrane.

B. Geometry

The geometry defines the spatial extent of the compartments defined in the physiological model. The geometry can be a compartmental geometry defining a ''whole-cell'' model, or an arbitrarily-shaped spatial geometry in any dimension. A spatial geometry is composed of one or more nonoverlapping regions. Regions are grouped according to the type of cellular structure they represent. Spatial geometries may be defined in terms of analytic functions or an image, or any combination of analytic functions and an optional image. An image, in our terminology, is a regularly sampled scalar field in one, two, or three dimensions. The geometry, therefore, is composed of one or more domains, enclosed in a bounding box that represents the simulation boundary.

Analytic functions are input using inequalities. For example, a spherical region representing a cell's nucleus could be specified as $x^2+y^2+z^2<10^2$. Furthermore, inequalities can be combined using Boolean logic (using the Boolean operator notation of the C programming language); for example, $x^2+y^2+z^2<10^2$ && $x>0$ could be used to slice the nucleus in half. Currently, the coordinate system used in these analytic functions is limited to Cartesian coordinates.

Segmented images are images where each color corresponds to a distinct type of cellular structure. Each contiguous region of the same color represents a domain in the geometry. Therefore, experimentally obtained images (typically 8- or 16-bit images) must be preprocessed before they can be used in geometry specifications. This preprocessing step usually involves only simple techniques found in most standard image processing packages: Sharpening, edge detection, thresholding, flood fill, etc. Once segmented, the images are imported into the Virtual Cell database, and are then available for use within the Virtual Cell. A three-dimensional geometry can be specified by a stack of two-dimensional images, each representing a slice through the three-dimensional geometry. In this case, the images are considered to represent consecutive slices through the three-dimensional geometry.

C. Simulation mapping

Once specified, the compartments of the physiological model can be mapped to groups of domains (e.g., multiple cells) comprising the goemetry. Extensive checking is performed to ensure that the topological constraints (parent–child relationships) inherent in the compartmental layout are preserved during the mapping. For example, if two compartments do not have a parent–child relationship between them, they may not be mapped to regions that share a common boundary. It is important to note that, until the physiological model is mapped to the geometry, it is not possible to define spatial parameters. We have therefore chosen to not allow any physiological parameters at all to be specified until the mapping has been performed. This constraint has the added benefit of making physiological models more reusable, as values such as rate constants (which tend to be cell- or preparation-dependent) are not introduced into the physiological model.

D. Running simulations and visualizing results

Once the physiological model and geometry have been mapped, and parameters have been set, simulations can be set up and run. This generally involves setting a small number of simulation parameters like the size of the computational mesh, the time step, and the interval between data storage steps. In the case of whole-cell models that are described by ordinary differential equations only, a number of numerical methods can be chosen: Euler's method, Runge–Kutta, Adams–Bashforth–Moulton, and Runge–Kutta–Fehlberg. We are also currently integrating a stiff solver, a modern adaptation of the Gear algorithm for systems of stiff algebraic and ordinary differential equations. Spatial models are solved using a finite volume approach on a structured grid; the details are discussed below in Sec. II. Once the simulation parameters have been fully specified, the simulation is run on a cluster of Compaq DS20 dual-processor workstations. Results are returned to the user as they become available, providing immediate feedback, and allowing the user to halt the simulation if things go awry.

Simulation results are stored in medium-term storage (up to several months, depending upon disk space limitations) for later retrieval and additional visualization. When simulation results are purged, however, all other model and simulation data are still maintained in the database, so that the results can be regenerated if needed at a later time by rerunning the simulation. We also provide tools for extracting data subsets, and exporting the data in a number of standard image, animation, and data formats. This allows for more detailed analysis, as well as the use of other visualization packages.

II. MATHEMATICAL FORMULATION

A. Governing equations

The central goal of the Virtual Cell is to perform *spatial* modeling of cell physiological processes. In spatial simulations, the nonlinear dynamics of interacting molecular species is combined with their diffusion, giving rise to a reaction–diffusion system mapped to arbitrary geometry with fluxes across membranes.[4] Mathematically, this translates into a system of coupled ''parabolic'' type partial differential equations with nonlinear reaction terms and flux boundary or jump conditions at the membranes.

For simplicity, let us consider a domain Ω containing one region Ω_{in} inside a cell and another region Ω_{out} outside the cell, separated by the cell membrane. Let $u_i, i=1,...,n$, be the concentrations of the various molecular species involved in cellular dynamics and governed by a system of reaction–diffusion equations

$$\frac{\partial u_i}{\partial t}=\nabla\cdot(D_i\nabla u_i)+R_i, \quad i=1,...,n, \tag{2.1}$$

in both Ω_{in} and Ω_{out}. Here D_i is the diffusion coefficient of the ith species. The effect of all the reactions on the ith species is represented by the source term R_i, which is a given function of $u_1,\ldots,u_n$. (The formulation also includes the option that a certain species exists only in a single region, say in Ω_{in}.) If some of the diffusion coefficients D_i are zero, we then have a system of coupled partial and ordinary differential equations.

Suppose there are m different reactions with rates ν_j, $j=1,...,m$, taking place among the various species. Usually each ν_j is a given nonlinear function of the concentrations of the species participating in this jth reaction. Then, if α_{ij} is the (i, j) element of the integer-valued stoichiometry matrix,[5] which represents how many molecules of the ith species are produced (the positive sign) or consumed (the negative sign) due to the jth reaction, we have

$$R_i=\sum_{j=1}^{m}\alpha_{ij}\nu_j. \tag{2.2}$$

However, at spatial scales on the order of a whole cell or larger, some physiological compartments (e.g., endoplasmic reticulum) are too small and convoluted to be spatially resolved. Such internal compartments may be distributed as a volume fraction of the region Ω_{in} of the enclosing compartment (e.g., cytosol). Membrane binding reactions and transmembrane fluxes of u_i that occur on the surface of these internal compartments are represented physically as molecular fluxes. These fluxes may be introduced as additional source terms for u_i within Ω_{in}.

Let the initial conditions

$$u_i(x,0)=u_i^0(x), \quad i=1,...,n, \quad x\in\Omega, \tag{2.3}$$

and the boundary conditions on $\partial\Omega$ be given. If for each species there is zero flux at the borders of the computational domain Ω, which is often the case, then

$$\nabla u_i\cdot\mathbf{n}=0 \quad \text{on} \quad \partial\Omega, \tag{2.4}$$

where $\mathbf{n}$ is the unit outward normal on $\partial\Omega$.

Due to the presence of the cell membrane, we need to impose jump conditions there, which relate the species concentrations on different sides of the membrane. Since second-order spatial derivatives are involved in the governing equations, we need two jump conditions across the membrane for each species with nonzero diffusion coefficient. Let the outside and the inside of the membrane be denoted by the subscript $-$ and $+$, respectively. For example, $u_i|_+$ represents the concentration of the ith species on the inside of the membrane. Let $\mathbf{n}$ be the outward unit normal on the membrane (i.e., pointing towards the outside of the cell). Then the jump conditions at the membrane are

$$\begin{aligned} -\nabla u_i|_+\cdot\mathbf{n}&=g_+(u_i|_+,u_i|_-),\\ -\nabla u_i|_-\cdot\mathbf{n}&=g_-(u_i|_+,u_i|_-), \end{aligned} \tag{2.5}$$

where $g_+,g_-:[0,\infty)\times[0,\infty)\to\mathbf{R}$ are typically given functions of $u_i|_+,u_i|_-$. However, depending on the physiological mechanisms involved, they can be functions of other variables as well. In the case a membrane cannot store a species, the flux in and out of the membrane must be the same due to mass conservation: $g_+=g_-\equiv g$. Equation (2.1) together with initial condition (2.3), boundary condition (2.4), and jump condition (2.5) determine the time evolution of the species dynamics.

B. Numerical algorithm

We now describe the numerical technique which is regularly applied in the Virtual Cell for solving the governing equations outlined in the previous section. In Virtual Cell applications, the computational domain Ω is always rectangular, and a structured orthogonal grid is utilized for spatial discretization.[6] This facilitates automatic sampling of cell geometry, particularly when it is based on experimental microscope images, where we can only tell whether a square pixel in the image lies inside or outside the cell, and also allows us to easily move from one-dimensional (1D) to two- (2D) to three-dimensional (3D) simulations. This kind of spatial discretization results in a ''staircase'' approximation of a cell membrane. The membrane elements of such a staircase are rectangular facets with normals parallel to the Cartesian axes. This creates difficulties for the accurate description of the membrane fluxes, because the surface area of the staircase does not converge to that of a real membrane when the mesh is refined. Moreover, a rotation of the coordinate system could substantially change simulation results.

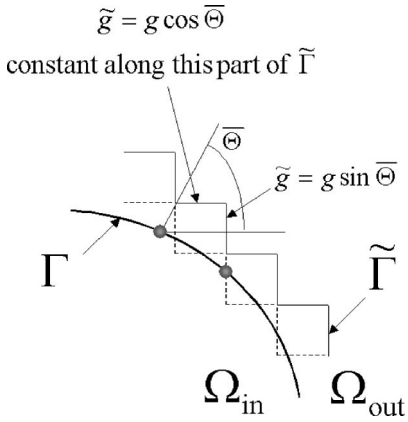

FIG. 2. Basic scheme for approximating boundaries. The regions Ω_{in} and Ω_{out} are separated by a membrane boundary Γ, which is approximated by the boundary $\tilde{\Gamma}$. The staircase shape of $\tilde{\Gamma}$ derives from the requirement that it must coincide with computational gridlines. Also shown is the scheme for interpolating jump conditions specified on Γ to gridpoints on $\tilde{\Gamma}$, as described in detail in the text.

As a simple example, suppose Ω_{in} to be a circle of radius 1 in $\mathbf{R}^2$. Now let $\tilde{\Omega}_{\text{in}}$ be any staircase approximation containing Ω_{in} (the area ''inside'' the staircase curve in Fig. 2). Then the exact membrane boundary Γ and its approximation $\tilde{\Gamma}$ have lengths of 2π and 8, respectively. With reaction terms $\nu_j=0$ and unit normal boundary flux per unit area on both Γ and $\tilde{\Gamma}$, call their solutions u_i and $\tilde{u}_i$, respectively. Then Eq. (2.1) give

$$\frac{\partial}{\partial t}\int_{\Omega}u_i=-2\pi D_i, \tag{2.6}$$

$$\frac{\partial}{\partial t}\int_{\tilde{\Omega}_{\text{in}}}\tilde{u}_i=-8D_i. \tag{2.7}$$

Thus, no matter how fine the staircase approximation is, the solutions in the two cases will differ immediately even if we start with similar initial conditions.

The above example suggests that a necessary condition for u_i and $\tilde{u}_i$ to be close to one another is that the total flux into both membranes Γ and $\tilde{\Gamma}$ have to be the same as the staircase domain is refined. To achieve this, we correct the flux across $\tilde{\Gamma}$. Let A_k be the area of the kth staircase membrane element. Because the flux density specified in (2.5) is meant to be normal to the real membrane Γ, the corrected flux density of the ith species across the kth membrane element is $g(u_i|_+,u_i|_-)\cos\theta_k$ where θ_k is the angle that the normal to Γ makes with the normal to the membrane element (here, for simplicity, we assume that the center of the element belongs to Γ, the more rigorous definition is given below). Hence the corrected flux across this membrane element will be $g(u_i|_+,u_i|_-)A_k\cos\theta_k$.

Since the exact normal is generally not known in applications, one has to employ some kind of an interpolation scheme to obtain a good estimate. In our practical implementation, we find it easier to ''correct'' the area of a membrane element: $\tilde{A}_k = A_k \cos\theta_k$ and store $\tilde{A}_k$ when sampling geometry. A rigorous analysis (see Appendix) shows that such membrane flux correction as described above ensures the convergence of $\tilde{u}_i$ to u_i in the model linear elliptic and parabolic cases. By constructing exact solutions for some nonlinear cases, our numerical tests also indicate convergence.

We now give a more detailed description of our flux (membrane) correction method using the 2D case for illustration purposes. Slightly more complicated bookkeeping is required for the 3D case. For simplicity, we drop the species number i dependence and let $g(\mathbf{x})$ denote the explicitly known value of $g_i(u_i(\mathbf{x}_+,t),u_i(\mathbf{x}_-,t))$ from the previous time step (see below for the discussion of time discretization). Let h be the grid size in the staircase approximation. First take many points $\overline{\mathbf{x}_i}$ along Γ so that the arc length between $\overline{\mathbf{x}_i}$ and $\overline{\mathbf{x}_{i+1}}$ is less than $2h$. For any point $\mathbf{x}\in\Gamma$, let θ be the angle that its normal makes with the x axis. Define $\overline{\theta_i}$ be the value of θ at $\overline{\mathbf{x}_i}$.

Each center point $\mathbf{x}$ of a horizontal or vertical segment in $\tilde{\Gamma}$ is at most $2\sqrt{2}h$ away from at least one $\overline{\mathbf{x}_i}$. Pick any $\overline{\mathbf{x}_i}$ in case there is a choice. Then for all $\mathbf{x}$ in this same segment, define the corrected flux

$$\tilde{g}(\mathbf{x}) = \begin{cases} g(\overline{\mathbf{x}_i})\cos\overline{\theta_i}, \\ \quad \text{if } \mathbf{x} \text{ is in the horizontal segment of } \tilde{\Gamma} \\ g(\overline{\mathbf{x}_i})\sin\overline{\theta_i}, \\ \quad \text{if } \mathbf{x} \text{ is in the vertical segment of } \tilde{\Gamma} \end{cases}. \quad (2.8)$$

As shown in the Appendix, such flux corrections on the staircase membrane ensure that $\tilde{u}_i$ converges to u in some norm.

For the interior points in Ω_{in} and Ω_{out}, we currently use a finite volume method[7] to implement an implicit backward difference time discretization[8] of the diffusion term, and an explicit treatment of the nonlinear reactions in Eq. (2.1). This gives us numerical stability, and avoids solving a large system of nonlinear equations, when the membrane jump conditions are also treated explicitly. The local discretization error is first order in time and second order in space. The backward difference discretization is usually derived by a finite difference approximation. However, the same scheme can be obtained as a consequence of the finite volume method,[7,9] which is numerically conservative. Unlike nonconservative numerical schemes that would give mass conservation only within a certain tolerance provided the spatial and temporal steps are small enough, the finite volume approach ensures exact mass conservation even when the grid size is coarse (so that solution may not be computed accurately) which is important in physiological applications. One can regard the finite volume method as a systematic way of arriving at a conservative finite difference type scheme.[9]

The zero boundary flux condition (2.4) on a rectangular domain Ω can be discretized in a standard way with second order accuracy.[8] As for the membrane Γ, the treatment, as discussed above, is more complicated and leads to a lower order of accuracy in space in our current implementation. To improve the overall convergence rate of the entire algorithm in the future, a necessary condition is a better reconstruction of the membrane location to generate an accurate analytical description. Various interpolation algorithms are being tested at this time.

The resulting system of linear algebraic equations is solved iteratively at each time step by the line-by-line method.[7] The size of this linear system is determined by the number of computational volumes (or grid points) and the number of species. For a typical application, more than 90% of the total computational time in the entire simulation is spent on the solution of the linear system. It is, therefore, worthwhile to invest some effort in improving the efficiency of the linear solver. We are currently experimenting with other iterative solvers based on Krylov iterative methods such as preconditioned conjugate gradients[10] with a preconditioner using incomplete factorizations. Preliminary tests show the reduction in computational time by at least a factor of 2 compared to the current line-by-line solver. We are also planning to test other preconditioners that take advantage of the special matrix structure, such as block and ADI preconditioners. The parallel implementation of these solvers would further improve the speed of computations. Some preliminary experiments conducted on alternating direction type solvers show encouraging speed-ups for a small number of processors. However, more work is needed before a decision can be reached on what combination of iterative solvers and parallel implementation will give the best flexibility and overall performance.

C. Fast processes in reaction–diffusion systems

Biological processes are generally composed of sets of events with vastly different time scales. Such multiple time scales in the systems of interest make the equations stiff. A regular algorithm will necessitate a small time step to resolve the fast time scale for its numerical stability, even though the actual physical phenomenon occurs at the slow time scale. Unless special precautions are taken, this will lead to expensive numerical calculations. We first consider systems with fast reactions and then briefly discuss the opposite limiting case when diffusion or other equilibrating processes (e.g., relaxation of charges to a membrane) are very fast.

Calcium dynamics is an example of a situation where a system contains reactions (calcium buffering) that are much faster than the other key elements, calcium diffusion, and fluxes from (and back to) the internal calcium stores.[11] In 1994 Wagner and Keizer developed the rapid buffer approximation to deal with this problem.[12] They used a pseudo-steady approximation to exclude ''fast variables'' and derived an effective transport equation for calcium. This equation, in general, is no longer of a reaction–diffusion type. Thus, we could not use this approach in our general framework directly because (1) it would require a user to do preliminary analytical work, which can often be quite involved, and, more importantly, (2) in each particular case the

final equations might be of different forms and require different algorithms. What we need is a general, purely numerical, approach that can be applied to any reaction–diffusion system with fast subsystems, no matter how complex its reaction scheme is.

We have developed such an approach,[13] which is based on the combination of time splitting[14] and a pseudo-steady approximation applied to the fast subsystem. In this approach, time splitting involves updating variables in two steps, separately for slow processes and for fast reactions. Thus, we always remain within a general reaction–diffusion scheme. In the current approach, to update variables in fast reactions, we use a pseudo-steady approximation; i.e., we replace ordinary differential equations with algebraic equations that reflect rapid equilibrium of fast reactions. At this point care must be taken in choosing a number of independent algebraic equations equal to the number of unknowns. This is achieved with stoichiometry analysis[5,15] that results in a coupled system of nonlinear algebraic equations and a set of linear constraints, corresponding to conservation relationships within the fast subsystem. It is important that the values of ''fast'' invariants are updated at each time step using results from solving ''slow'' equations. The stoichiometry analysis is performed automatically within our framework after a user specifies which reactions are considered fast.

We now describe our algorithm in more detail.[13] Without loss of generality, let the first k reactions be fast with rates $\nu_1,\ldots,\nu_k, k\leqslant m$, respectively, while the remaining $m-k$ reactions are slow with rates $\nu_{k+1},\ldots,\nu_m$, respectively. Diffusion is assumed to be a slow process which is usually the case in the length scale of interest. A typical time step, say from T to $T+\Delta t$, is advanced in two stages. In both stages, the equations are coupled due to the reaction rate ν_j, $j=1,...,m$.

Stage I: Due to fast reactions. We solve

$$\frac{\partial u_i}{\partial t}=\sum_{j=1}^{k}\alpha_{ij}\nu_j, \quad i=1,...,n, \tag{2.9}$$

with given initial condition $u_i(\mathbf{x},T)$, $i=1,...,n$, $\mathbf{x}\subset\mathbf{R}^3$. Its actual implementation involves the pseudo-steady approximation and will be discussed below. We let their solution be $\tilde{u}_i(\mathbf{x})$, $i=1,...,n$, after a time of Δt.

Stage II: Due to slow reactions and diffusion. Using the regular algorithm discussed above, we solve

$$\frac{\partial u_i}{\partial t}=D_i\nabla^2 u_i+\sum_{j=k+1}^{m}\alpha_{ij}\nu_j, \quad i=1,...,n, \tag{2.10}$$

with the same boundary and jump conditions as for the governing equations and initial conditions $\tilde{u}_i(\mathbf{x})$ from the results in Stage I. The result that we obtain after a time of Δt is our numerical approximation to $u_i(\mathbf{x},T+\Delta t)$. We then repeat stage I and II to compute the solution at successive times.

In Stage I, Eq. (2.9) involves the $n\times k$ stoichiometry matrix $\alpha^{(f)}\equiv\alpha_{ij}$, $1\leqslant i\leqslant n$, and $1\leqslant j\leqslant k$. Assume the rank of the matrix $\alpha^{(f)}$ to be r, therefore, $r\leqslant\min(n,k)$. Its left null space $\mathcal{N}((\alpha^{(f)})^T)$ has a dimension of $n-r$, with a basis $\{\mathbf{l}_1,\ldots,\mathbf{l}_{n-r}\}\subset\mathbf{R}^n$. Using (2.9), it is then easy to verify that $\partial/\partial t(\mathbf{l}_i\cdot\mathbf{u})=0$, where $\mathbf{u}=(u_1,\ldots,u_n)^T$. Hence for fixed $\mathbf{x}$

$$\sum_{j=1}^{n}\beta_{ij}u_j=I_i, \quad i=1,...,n-r, \tag{2.11}$$

where β_{ij} is the jth component of the vector $\mathbf{l}_i$, and I_i is constant during this time step (but depend on $\mathbf{x}$), which should be updated from the initial conditions in Stage I. Equation (2.11) represent all the conservation relations among the species with respect to fast reactions.

Next we employ the pseudo-steady approximation on the fast subsystem, i.e., we assume that the fast reactions are in equilibrium at all times. Consider the usual scenario when $r=k\leqslant n$. This approximation amounts to neglecting the time derivative in Eq. (2.9), and results in

$$\nu_i=0, \quad i=1,...,k. \tag{2.12}$$

Together with Eq. (2.11), they form a system of n nonlinear equations for n unknowns: u_i, $i=1,...,n$. We then use the linear equation (2.11) to reduce it to k nonlinear algebraic equation (2.12) and k unknowns, and solve them using Newton's method, with a good initial guess from the initial conditions for u_i in Stage I. For the general case when $r<k$, a particular choice of ''independent'' ν_i is required to extract r equations out of a total number of k. Details are again given in Ref. 13.

The pseudo-steady approximation has its scope of applicability. Obviously, it gives accurate results if the ratio of characteristic times of fast and slow processes is small. In fact, our results indicate that the relative error introduced by the approximation is roughly of the order of this ratio.[13] Therefore, the approximation may be appropriate if the characteristic times differ by two or more orders of magnitude. However, in nonlinear systems this ratio may vary in the process and, therefore, this condition might be violated. In formal singular perturbation language, there might be interior layers in the solutions with rapid change of variables. In case one would like to resolve the interior layers, more accurate approaches should be used. We still can take advantage of time splitting that allows us to break the problem into a number of manageable simpler sub-problems, that are studied in a vast amount of literature. For example, we can treat the reaction terms in Stage I with a stiff solver that will save substantially as compared to a non-stiff version. However, the pseudo-steady approximation, when it works, will save even more as it eliminates the fast time scale.

Because we break down the original governing equations in a typical time step Δt into two simpler steps (Stages I and II), the time splitting error is present even if we solve the simpler equations (2.9) and (2.10) exactly. The additional source of error coming from implementing the regular algorithm in Stage II was discussed in the previous section. In our actual numerical experiments, overall numerical stability and convergence are observed, with an overall accuracy of first order in time. The application of our algorithm to studying the effect of fast buffering on calcium waves in bistable models is described below in Sec. III B.

We now briefly discuss the opposite limiting case where diffusion of some molecular species is very fast compared to reactions and membrane fluxes. In this case, the corresponding concentration u_i is virtually uniform within a closed region (Ω_{in} in Fig. 2) at any time, so that there is no need to calculate its value for each elementary volume inside the region. Instead, the whole region Ω_{in} can be characterized by a single value u_i^{in} governed by an ordinary differential equation. This equation can be easily derived from Eq. (2.1) by integrating over Ω_{in} and taking into account the membrane jump condition (2.5)

$$\frac{\partial u_i^{\text{in}}}{\partial t}\int_{\Omega_{\text{in}}} d\Omega = -\int_{\Gamma} D_i g_+ d\Gamma + \int_{\Omega_{\text{in}}} R_i d\Omega. \tag{2.13}$$

We have recently incorporated the approximation (2.13) in the Virtual Cell. The actual implementation uses a concept of a *region* variable, a discrete type variable defined on a set of volume or membrane regions. Note that in the case of nonneuronal cells, the membrane potential falls into a category of a region variable defined on membranes. Thus, the new capability will allow a user to combine the dynamics of the membrane potential with the spatially resolved dynamics of species concentrations.

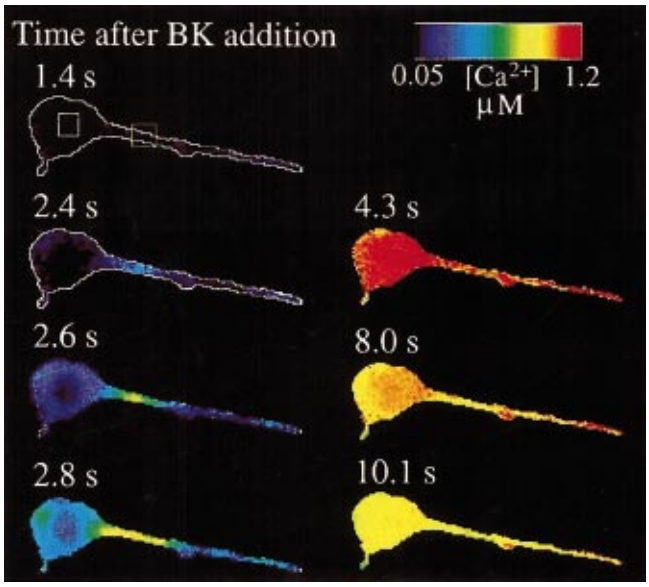

FIG. 3. (Color) BK-induced calcium wave in an N1E-115 neuroblastoma cell. BK (500 nM) was applied externally to the bathing medium of a cell stained with fluorescent dye (fura-2), and the fluorescence signal was collected. In these images, calcium is displayed in pseudocolor, as shown in the colorbar.

III. EXAMPLES OF THE VIRTUAL CELL APPLICATIONS TO CALCIUM DYNAMICS

Calcium oscillations and waves play an important role as a prerequisite for triggering a number of physiological processes such as hormone secretion, cell division, muscle contraction, etc.[16] One of the key elements of intracellular calcium dynamics is calcium release from the endoplasmic reticulum (ER), an internal calcium store, through calcium channels that can be activated by cytoplasmic calcium as well as by other signaling molecules that are present in the cytoplasm, such as inositol-1,4,5-trisphosphate (IP_3). Two other components of the calcium flux across the ER membrane are direct leak through the membrane and calcium uptake by molecular pumps—the proteins embedded in the membranes that pump calcium ions back into the ER against its gradient. The calcium concentration in the ER is several orders of magnitude higher than that in the cytoplasm; therefore, for many purposes the store can be considered to have infinite capacity. The ER has a very complex, irregular geometry.[17] Being a continuous closed compartment, it fills a cell with generally nonuniform density while occupying only ~15% of the cell volume. In a continuous approximation, it can be modeled by calcium sources and sinks continuously distributed with a certain density throughout a cell and characterized by certain rates. When combined with calcium diffusion, they give rise to a reaction–diffusion type equation[11]

$$\frac{\partial c}{\partial t} = \nabla(D_c \nabla_c) + f, \tag{3.1}$$

where c is the calcium concentration, D_c is the calcium diffusion coefficient, and $f = J_{\text{channel}} - J_{\text{pump}} + J_{\text{leak}}$ is the rate of change of calcium concentration due to fluxes through calcium channels, pumps, and leak. Calcium fluxes across the outer membrane may also influence calcium dynamics and can be taken into account through the appropriate boundary conditions.

A. An image-based model of calcium waves in differentiated neuroblastoma cells

Application of bradykinin (BK) to differentiated N1E-115 neuroblastoma cells elicits a single, transient release of calcium from internal stores via an IP_3-dependent pathway. This rise is in the form of a wave, and is highly reproducible from cell to cell. The point of origin is typically the middle of the neurite, and the wave travels in both directions down the neurite, ultimately filling the soma. Recovery follows the same pattern, the calcium concentration declining first at the wave initiation site, and spreading out along the neurite and into the soma. A typical BK-induced calcium wave is shown in Fig. 3.

BK is believed to initiate the calcium response through a g-protein cascade that leads to activation of phospholipase C and the phosphorylation of phosphatidyl inositol-4,5-bisphosphate (PIP_2) to IP_3. The IP_3 diffuses through the cytosol to the ER, where it activates calcium release through the IP_3 receptor calcium channel. The released calcium raises the free calcium concentration, but also binds to both fixed and mobile endogenous cytosolic calcium buffers. Cytosolic calcium is then pumped back into the ER via sarcoplasmic–endoplasmic reticulum calcium ATPase (SERCA) pumps.

The IP_3 receptor is a tetramer composed of four subunits, each of which has three binding sites: One for IP_3, and two for calcium. Binding of IP_3 is considered a prerequisite for subunit activation, whereas calcium acts as a coagonist for the IP_3 receptor: One calcium binding site activates the subunit, whereas the other site inactivates the subunit. In order to fit experimental data, it is assumed that three subunits

must be in the activated state for the channel to be open.

Our model for IP_3 dynamics[18,19] includes production at the plasma membrane, at a rate proportional to the level of BK receptor stimulation, and degradation within the cytosol. We model IP_3 dynamics as a reaction–diffusion process

$$\frac{\partial[\mathrm{IP_3}]}{\partial t} = D_i \nabla^2 [\mathrm{IP_3}] - k_i([\mathrm{IP_3}] - [\mathrm{IP_3}]_0), \tag{3.2}$$

where D_i is the diffusion constant of IP_3, k_i is the degradation rate of IP_3, and $[IP_3]_0$ is the basal IP_3 concentration. We model the BK receptor by assuming that IP_3 production is a function of receptor stimulation. Since this is restricted to the plasma membrane, this enters in as a boundary condition for $[IP_3]$

$$\frac{d[\mathrm{IP_3}]}{dn} = J_i \exp - k_i t. \tag{3.3}$$

From this equation, it should be clear that IP_3 production is turned on at $t=0$, decreasing in time with rate constant k_i. Note that J_i is a function of space, as it contains the density of BK receptor.

A number of experimental and modeling studies have shown that the binding to the inactivating calcium site is the slowest binding process.[20] This leads to the following model:

$$\frac{\partial[\mathrm{Ca^{2+}}]}{\partial t} = D_c \nabla^2 [\mathrm{Ca^{2+}}] + \sigma(J_{\mathrm{channel}} - J_{\mathrm{pump}} + J_{\mathrm{leak}}) + R_{\mathrm{buffers}}, \tag{3.4}$$

where

$$J_{\mathrm{channel}} = J_{\max}\left(\left(\frac{[\mathrm{IP_3}]}{[\mathrm{IP_3}] + K_{\mathrm{IP_3}}}\right)\left(\frac{[\mathrm{Ca^{2+}}]}{[\mathrm{Ca^{2+}}] + K_{\mathrm{act}}}\right) h\right)^3 \times \left(1 - \frac{[\mathrm{Ca^{2+}}]}{[\mathrm{Ca^{2+}}]_{\mathrm{ER}}}\right), \tag{3.5}$$

is the flux through the IP_3 receptor. In this formulation, the faster activation processes (activating calcium and IP_3 binding to the receptor) are assumed to be infinitely fast. Their binding to the subunits is, therefore, represented as always being at equilibrium, giving rise to the first two factors in J_{channel}. The channel state h represents the fraction of channel subunits not yet inactivated by calcium, and introduces the slow time scale into the model. The SERCA pumps are responsible for refilling the stores following calcium release, but are also important in maintaining low basal calcium levels at equilibrium. The flux due to the pumps, J_{pump}, is modeled as a Hill function

$$J_{\mathrm{pump}} = V_{\max} \frac{[\mathrm{Ca^{2+}}]^2}{[\mathrm{Ca^{2+}}]^2 + K_p^2}, \tag{3.6}$$

where $V_{\max}$ is the maximal pump rate, and K_p is the calcium concentration at which the pump rate is half maximal. Both the functional form and the parameter values used are in agreement with experimental measurements on SERCA Type 2(B) pumps. Finally, we also include a small, passive leak from the ER to the cytosol

$$J_{\mathrm{leak}} = L\left(1 - \frac{[\mathrm{Ca^{2+}}]}{[\mathrm{Ca^{2+}}]_{\mathrm{ER}}}\right). \tag{3.7}$$

Our model also includes several cytosolic calcium buffers: Stationary buffers representing endogenous buffers like calcium-binding proteins, and mobile buffers representing the fluorescent dyes used in our experimental measurements. The details of how these buffers are treated are covered in depth below, and are left out of this discussion for brevity.

In addition to calcium regulation and release, our model includes two additional features: Realistic cellular geometry, and experimentally determined spatial variation in the distribution of ER, IP_3 receptors and SERCA pumps. As discussed below, both turned out to be critical to our understanding of the BK-induced waves.

The cellular geometries used were derived from fluorescence microscope images of actual cells, for example, that shown in Fig. 3. Indeed, in cases where comparisons between experiment and model were made, the models incorporated the geometry of the actual cell used in the experiment. We used the Virtual Cell's image-based geometry features to input the geometries, and to identify two spatial regions: The intracellular space, and the extracellular space. Both the cytosol and the ER were mapped to the intracellular space, and the ER was assigned a spatially varying volume density, relative to the volume of the cytosol. This allows us to treat the ER as a distinct compartment without having to specify its complicated geometrical shape.

Our model also allows for the spatial variation of the distributions of the ER, IP_3 receptors, SERCA pumps and BK receptors. In order to estimate these distributions, we performed immunofluorescent staining on fixed cells, and reconstructed their three-dimensional distributions; Fig. 4 shows a volume rendering of the three-dimensional distribution of SERCA pumps in an example N1E-115 Nb cell. These reconstructions were then analyzed to compute the relative fluorescence intensities in six regions of each cell: Distal soma, proximal soma, proximal neurite, middle neurite, distal neurite, and growth cone. These data were then corrected for relative blurring, and the corrected relative intensities ($\sim$20 cells per immunostain series) were then mapped onto the cellular geometry used for each simulation. Figure 5 shows the mapping of ER density (in the interior) and BK receptor (along the plasma membrane) for an example cell. Our analyses showed that the relative distributions of ER, IP_3 receptors and SERCA pumps were statistically indistinguishable ($p<0.05$), indicating that both the IP_3 receptors and SERCA pumps were uniformly distributed on the ER membrane. Table I shows the mean relative distributions (and standard deviation and standard error) of ER and BK receptors, subdivided into the six cellular regions. All simulations used these values, with variations up to but not exceeeding one standard deviation in order to fit the accompanying experiments.

Figure 6 shows experimental and simulation results for the BK-induced calcium wave in two different N1E-115 Nb cells using ''best-fit'' parameter values (see Ref. 18 for actual values used), with the relative distributions of ER, IP_3 receptors, SERCA pumps and BK receptors within one stan-

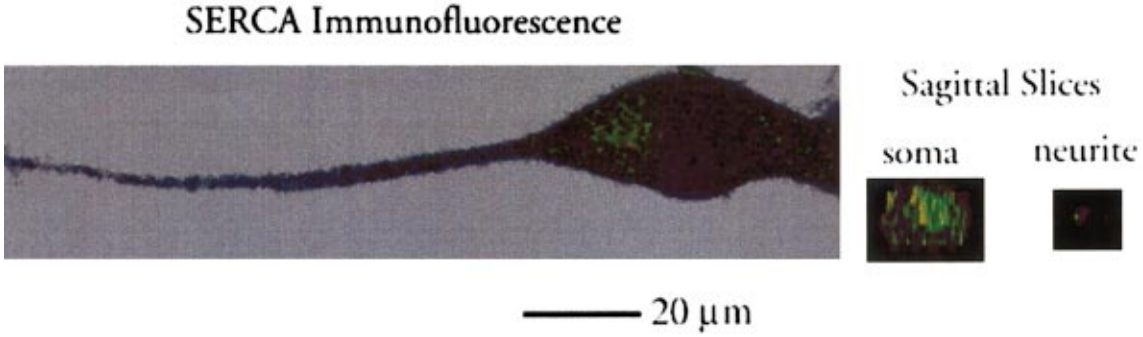

FIG. 4. (Color) Example of a 3D immunofluorescence image used to determine intracellular distributions. In the example, an N1E-115 neuroblastoma cell has been fixed and stained with an antibody to SERCA 2.

dard deviation of the means given in Table I. Following application of BK (at $t=0$), IP_3 accumulates rapidly in the neurite, and to a lesser extent, in the soma and distal neurite. Calcium and the newly produced IP_3 open the IP_3 receptors cooperatively, initiating a bidirectional wave of increased calcium concentration. The calcium wave spreads with approximately uniform maximal amplitude ($\sim 1.2\ \mu M$). The elevated calcium then closes the IP_3 receptors, and $[IP_3]$ falls back to basal levels due to IP_3 degradation. The SERCA pumps then restore basal calcium levels, pumping cytosolic calcium back into the ER.

The simulation shown in Fig. 6(a) is of a bipolar N1E-115 neuroblastoma cell. In these calculations, we assumed a symmetrical model: Both neurites contain ER and BK receptor distributions using mean values from Table I, while the center of the soma is assigned a relative density of unity. Comparison with the experimental images shows remarkably good agreement in a number of key features: The location of wave initiation, the bidirectional wave propagation, the spread of the wave from neurite to soma, maximal amplitude of cytosolic calcium concentration, and clearance of calcium from the cytosol.

Figure 6(b) shows calculations in an aster-shaped neuroblastoma cell. In these simulations, the BK receptor density was uniform, and the ER density in the periphery was set to 60% of a central circle, and the nuclear region was void of ER. In this case, the fit to experiment was more qualitative than quantitative. The wave is initiated in the neurite, and spreads rapidly into the soma. However, the maximal amplitude of calcium concentration in the soma, and the rate of recovery do not match the accompanying experiment. We speculate, however, that the simulations could be made to more quantitatively match the experiment with rather small parameter changes reflecting population variances.

The two main features of the Virtual Cell illustrated in this example are the ability to specify cellular geometry using experimental images, and the ability to change the geometry easily and without modifying the physiological model. The utility of these two features is apparent in Fig. 6: By varying realistic geometries, we can draw conclusions about the BK induced calcium wave that are independent of cellular geometry (e.g., the wave is generally initiated in the neurite).

B. Buffered calcium waves in bistable systems

Calcium buffering is now widely recognized to have a strong impact on the overall intracellular calcium dynamics.[21,22] In addition to endogenous buffers (mainly proteins with calcium binding sites) that are always present in a cell, there is another reason that makes the study of the buffer effect on calcium dynamics very important. In experimental studies, calcium dynamics are visualized by loading a cell with a fluorescent indicator that acts as a high affinity mobile buffer. It is, therefore, crucial to know to what extent the exogenous buffer (a fluorescent indicator) can distort the original pattern.

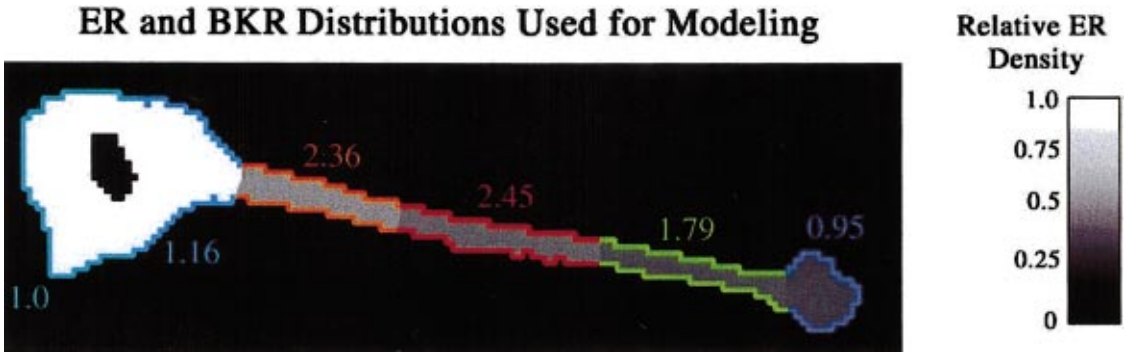

FIG. 5. (Color) Intracellular distributions of BK receptor and ER/IP_3 receptor/SERCA 2, projected onto the morphology of the cell in Fig. 4. The relative BK receptor surface densities along the plasma membrane for the six averaged regions of the cell are shown in color-coding along the periphery; the average distribution of the ER is identical to that of IP_3 receptor and SERCA, and is shown as gradations of gray values within the cell with a scale indicator on the right. In both cases, densities are expressed relative to the leftmost section of the soma taken as unity.

TABLE I. Relative distributions of ER and BK receptors.

Region	ER distribution			BKR distribution		
	Mean	SE	SD	Mean	SE	SD
Outer soma	1.00	0.00	0.00	1.00	0.00	0.00
Inner soma	1.03	0.02	0.13	1.16	0.03	0.13
Proximal neurite	0.67	0.04	0.25	2.36	0.16	0.72
Mid neurite	0.60	0.04	0.24	2.45	0.22	0.97
Distal neurite	0.58	0.04	0.23	1.79	0.18	0.81
Growth cone	0.53	0.04	0.23	0.95	0.09	0.38

We have applied our approach[13] to fast reactions in reaction–diffusion systems (see Sec. II C) to study the effect of fast mobile buffers on calcium waves in bistable systems [Fig. 7 shows the typical behavior of the function $f(c)$ in Eq. (3.1) for one-variable systems] that are known to maintain stable self-propagating waves.[23] Moreover, bistability is thought to be essential in the phenomenon of fertilization calcium waves.[24] It is important for bistability that $f(c)$ has three zeros $C_{\min}<C_0<C_{\max}$, which in the absence of diffusion would correspond to the concentration values in two

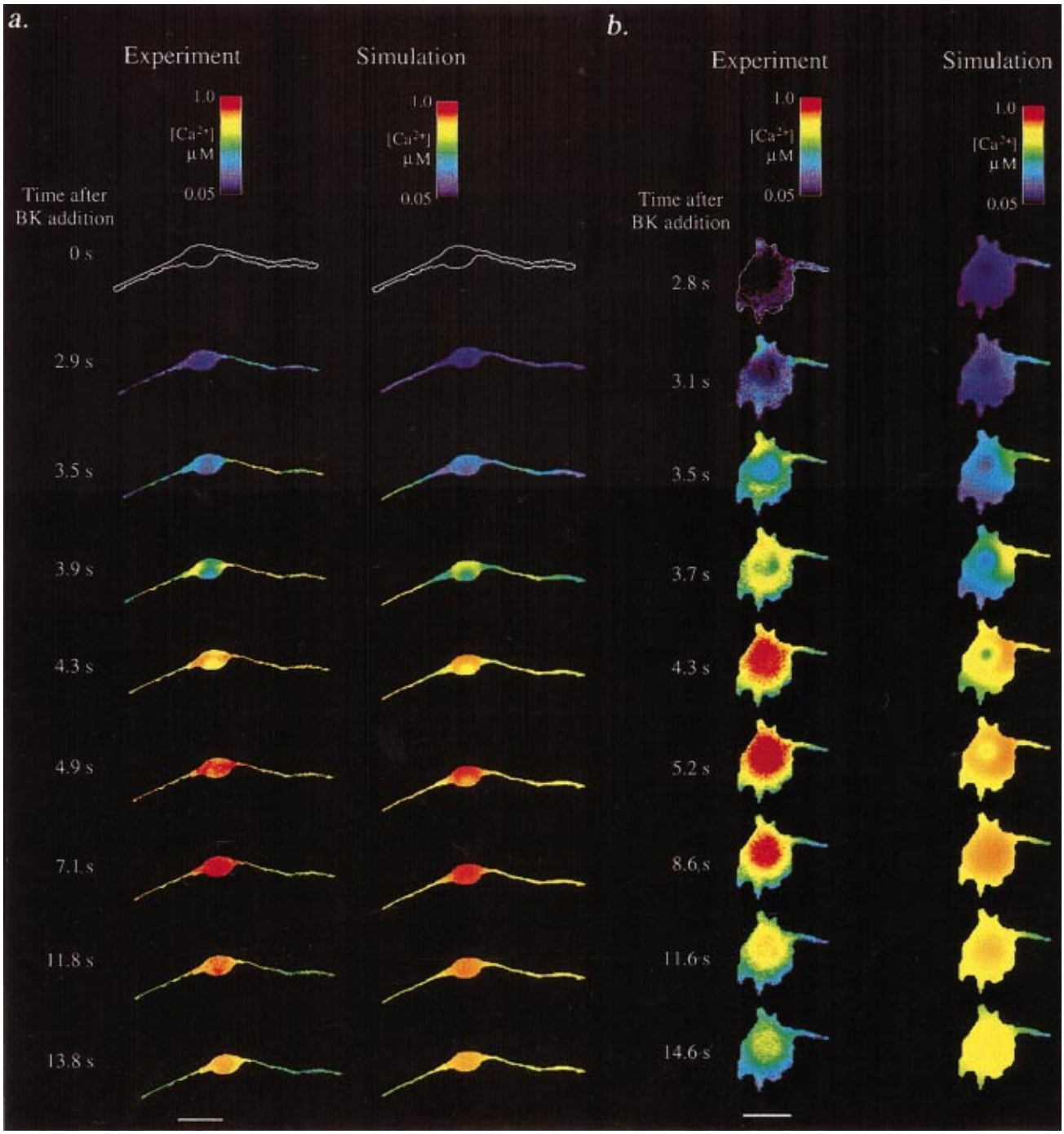

FIG. 6. (Color) Experimental and simulation BK-induced calcium release in N1E-115 neuroblastoma cells of differing morphology. Cells were loaded with fura-2 and imaged as in Fig. 4. (a) Intracellular distributions were modeled as in Fig. 5 but with two neurites instead of one. (b) BK receptor and ER were modeled as having uniform distributions throughout the cell except for the small fingerlike nascent neurite, which was assigned lower ER densities consistent with Fig. 5. Scale bars: (a) 50 microns, and (b) 20 microns.

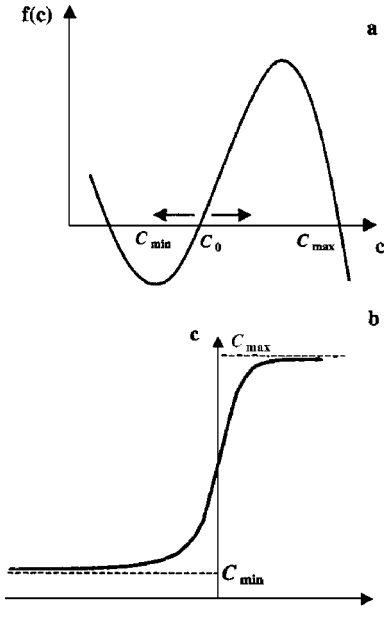

FIG. 7. (a) Typical shape of the function f in one-variable bistable models. (b) Typical traveling wave profile in one-variable models.

stable steady states separated by an unstable steady state. In physiological applications the system usually rests at a steady state with lower concentration $C_{\min}$. Thus, to excite the system, we have to overcome the concentration barrier $C_0 - C_{\min}$. Therefore, the position of the unstable steady-state concentration C_0 with respect to $C_{\min}$ and $C_{\max}$ characterizes the system excitability.

In the absence of buffers, one can derive a general implicit expression for the wave speed v of a traveling wave type solution $c(x+vt)=c(\xi)$ in a one-variable bistable system[4]

$$v=\left(\int_{C_{\min}}^{C_{\max}} f(c)dc\right)\left(\int_{-\infty}^{\infty}\left(\frac{dc}{d\xi}\right)^2 d\xi\right)^{-1}. \tag{3.8}$$

In the presence of a mobile buffer interacting with calcium according to the reaction

$$C_a + B \rightleftharpoons C_a B, \tag{3.9}$$

where B and CaB denote the free and bound forms of the buffer, the system is described by the set of equations

$$\begin{aligned}
&\frac{\partial c}{\partial t} = D_c \nabla^2 c + f + R,\\
&\frac{\partial b}{\partial t} = D_b \nabla^2 b - R,\\
&R = -k_{\text{on}} c(b_t - b) + k_{\text{off}} b,
\end{aligned} \tag{3.10}$$

where $b=[CaB]$, D_b is the buffer diffusion coefficient, k_{on} and k_{off} are the reaction kinetic constants, and the total buffer concentration $b_t=[B]+[CaB]$ is conserved at each spatial point for any $t>0$ if we assume zero flux boundary conditions for the buffer,the same diffusion coefficients for both forms of the buffer, and initially spatially uniform buffer distribution. As we mentioned above, calcium buffering is considered to be much faster than other components affecting calcium dynamics, so the pseudo-steady approximation can be applied and the set of reaction parameters reduces to the buffer dissociation constant $K \equiv k_{\text{off}}/k_{\text{on}}$. (Here, [B] and [CaB] are the concentrations of the free and bound forms of the buffer, respectively.)

According to theorem 2.1, in Ref. 25, the system (3.10) allows for the monotone traveling wave solutions connecting two stable steady states and a unique wave speed. For this case, it is also possible to derive the general expression for the wave speed, somewhat analogous to Eq. (3.8)[13]

$$\begin{aligned}
v=&\left(\int_{C_{\min}}^{C_{\max}} f(c)\left(1+\frac{D_b b_t K}{D_c (K+c)^2}\right)dc\right)\\
&\times\left(\int_{-\infty}^{\infty}\left(1+\frac{b_t K}{(K+c)^2}\right)\left(1+\frac{D_b b_t K}{D_c (K+c)^2}\right)\left(\frac{dc}{d\xi}\right)^2 d\xi\right)^{-1}.
\end{aligned} \tag{3.11}$$

In the limit of low buffer affinity $K/C_{\max} \gg 1$ this equation can be shown[13] to reduce to a well-known expression for the wave speed[26]

$$v = v_0\left(1+\frac{D_b b_t}{D_c K}\right)^{1/2}\left(1+\frac{b_t}{K}\right)^{-1}, \tag{3.12}$$

where v_0 is the speed of a wave in the absence of buffering.

Although Eq. (3.11) is not explicit, one can get some important insights by analyzing it. Define $\gamma \equiv D_b b_t / D_c$. Let us fix $C_{\min}$ and $C_{\max}$ and vary the system excitability by changing C_0. To emphasize this fact, we write $f(c) \equiv f(c, C_0)$. Then from Eq. (3.11), the sign of the wave speed (and, consequently, the condition for the existence of the traveling wave with the domination of the higher steady-state concentration) is determined by the sign of the integral

$$V \equiv \int_{C_{\min}}^{C_{\max}} f(c, C_0)\left(1+\frac{\gamma K}{(K+c)^2}\right)dc, \tag{3.13}$$

which depends both on system excitability and buffer characteristics. This is in agreement with the result of Ref. 26 obtained by means of a particular nonlinear transformation. We further define

$$G(C_0) \equiv \int_{C_{\min}}^{C_{\max}} f(c, C_0)dc,$$

$$H(C_0, K) \equiv \int_{C_{\min}}^{C_{\max}} \frac{f(c, C_0)}{(K+c)^2}dc.$$

If $\partial f/\partial C_0 < 0$, which is true, for instance, in the case of a cubic polynomial, $f(c)=(J_0/C_{\max}^3)(c-C_{\min})(c-C_0)(C_{\max}-c)$, then $\partial G/\partial C_0 < 0$ and $\partial H/\partial C_0 < 0$. Hence there are unique values of C_0, $\overline{c}$, and $\tilde{c}=\tilde{c}(K)$, such that $G(\overline{c})=0$ and $H(\tilde{c}, K)=0$. Since $H(\overline{c}, K)<0$, then $\tilde{c} \in (C_{\min}, \overline{c})$ and $\tilde{c}$ tends to $\overline{c}$ as K increases.

We now fix K and consider any $C_0 \in (C_{\min}, \tilde{c}]$ (high excitability regime); then the integral (3.13) is positive irrespective of the value of γ. In other words, the traveling wave speed is always positive no matter what total buffer concentration we introduce and how large its diffusion coefficient

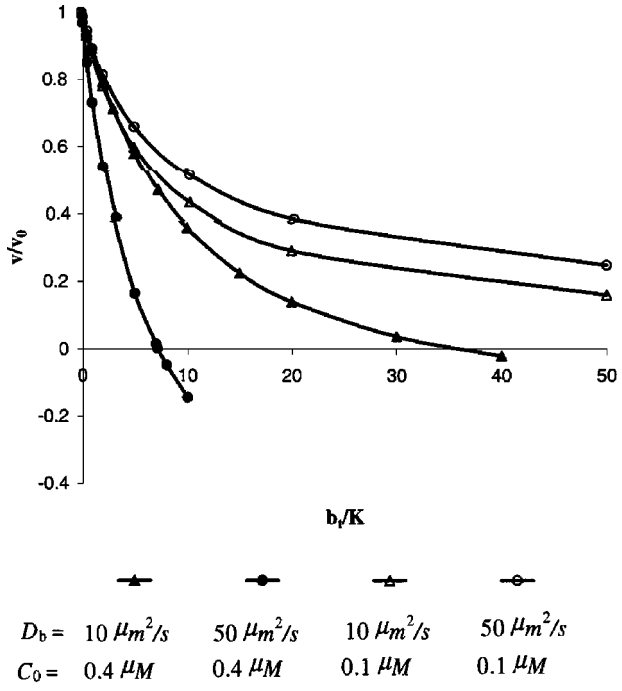

FIG. 8. Results of 1D simulations for the cubic polynomial model: The normalized wave speed vs buffer binding ratio for varying system excitability and buffer diffusion at $K=0.1\ \mu$M. While decreasing with the growing total buffer concentration, the wave speed stays positive at high system excitability ($C_0=0.1\ \mu$M) and becomes negative beyond some threshold at low system excitability ($C_0=0.4\ \mu$M). The dependence of the wave speed on the buffer diffusion coefficient is increasing at high excitability and decreasing at low excitability. In these calculations, $C_{\min}=0\ \mu$M, $C_{\max}=1.0\ \mu$M, and $J_0=20\ \mu$M/s.

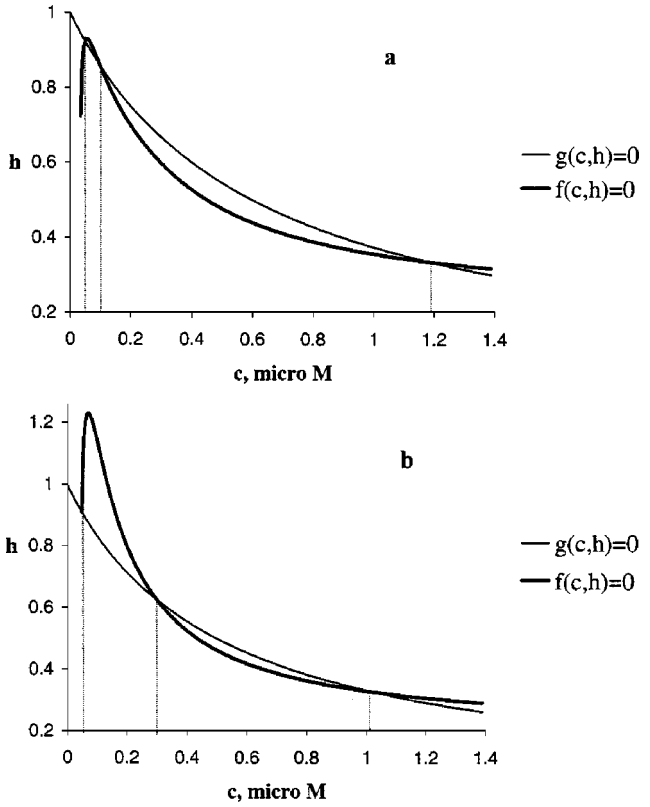

FIG. 9. Nullclines of the Li–Rinzel model for the cases of high (a) and low (b) excitability.

is, as long as the system excitability is sufficiently high. On the other hand, when $C_0\in(\tilde{c},\overline{c})$ (the low excitability regime), there is a threshold value of γ

$$\gamma C_0 \equiv -\frac{1}{K}\frac{G(C_0)}{H(C_0,K)}, \tag{3.14}$$

such that for $\gamma>\gamma_{C_0}$, there are no traveling waves with positive speeds. If $C_0\geqslant\overline{c}$, the wave speed is negative (the lower steady-state concentration dominates) for any combination of buffer parameters.

It is interesting to note that the dependence of the numerator in Eq. (3.11), V, on D_b is drastically different in regions of high and low excitability: For $C_0<\tilde{c}$ the wave speed v is positive and $\partial V/\partial D_b>0$, while for $C_0\in(\tilde{c},\overline{c})$, $\partial V/\partial D_b<0$. Thus, in situations when the numerator of Eq. (3.11) plays a dominant role in determining the wave speed, an increase of the buffer diffusion coefficient may speed up or reduce the wave velocity in the high- and low-excitability modes, respectively. In the low-affinity limit $K/C_{\max}\to\infty$, when the low-excitability region is disappearing because $\tilde{c}\to\overline{c}$, we expect the wave speed to be an increasing function of D_b for any $C_0\in(C_{\min},\overline{c})$, in accordance with Eq. (3.12). However, in the case of a high affinity buffer and low-system excitability ($C_0\in(\tilde{c},\overline{c})$), this dependence might be the reverse. In this case, the growth of D_b will lead to a point $\gamma=\gamma_{C_0}$ at which the traveling wave with a positive wave speed ceases to exist. Our numerical results (Fig. 8) obtained from 1D simulations for the cubic polynomial confirm such a conclusion.

Although the simple analysis, valid for one-variable bistable models, does not apply in multivariable bistable models, most of the qualitative conclusions appear to hold in a more realistic Li–Rinzel model[20] which has been successfully applied in the studies of calcium dynamics.[18,19,24] In the absence of a mobile buffer, the model contains two variables: The calcium concentration, c, and the probability h that the inhibition site of a channel subunit is free of calcium. The model, given by the equations

$$\begin{aligned}\frac{\partial c}{\partial t}&=D_c\nabla^2 c+f(c,h),\\ \frac{\partial h}{\partial t}&=g(c,h),\end{aligned} \tag{3.15}$$

is bistable for some parameter sets,[13,24] and we again consider two modes when the unstable steady-state concentration C_0 is close to and far from the low steady-state calcium concentration $C_{\min}$ (Fig. 9). We will call them again the modes of high and low excitability, respectively, assuming that, as in one-variable models, the relative location of steady-state concentrations [for Eqs. (3.15) without diffusion] controls the system excitability.

Our numerical results show that, similar to the one-variable models, the buffer effect on the speed of a traveling wave strongly depends on the system excitability. In the high excitability mode, the wave speed increases with the buffer diffusion coefficient and will never become negative (Fig.

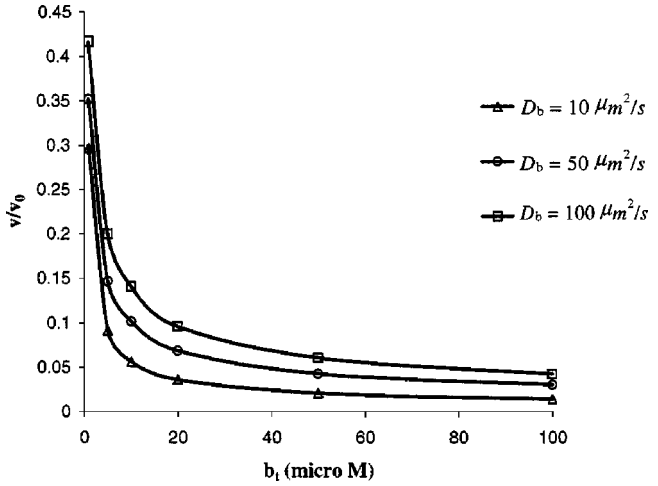

FIG. 10. Wave speed dependencies on the total concentration of a high-affinity buffer ($K=0.1\ \mu$M) at varying buffer diffusion coefficient in the high-excitability mode of the Li–Rinzel model.

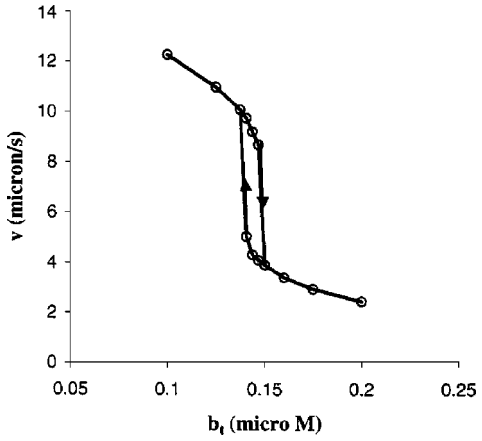

FIG. 12. Hysteresis loop in the wave speed dependence on the total buffer concentration in the low excitability mode of the Li–Rinzel model, at $K=0.1\ \mu$M and $D_b=50\ \mu\text{m}^2/\text{s}$.

10). For the low-excitability mode (Fig. 11), the wave speed is a decreasing function of the buffer diffusion coefficient at a fixed total buffer concentration. When the total buffer concentration exceeds a critical level, the wave speed becomes negative as in the one-variable models.

In this model, however, with increasing total buffer concentration, we observe a sudden drop of wave speed preceding the change in the wave direction (Fig. 11). Thus, there is a finite interval of wave speed values for which no stable traveling wave exists. On the other hand, if we start with a wave profile, corresponding to a high total buffer concentration, and then gradually decrease the buffer concentration in our simulations, the jump occurs at a lower critical value resulting in a typical hysteresis loop presented in Fig. 12, which is a magnified picture of the middle curve in Fig. 11 near its discontinuous jump. Therefore, for a fixed buffer diffusion coefficient, there are at least two stable traveling waves with very different velocities when the total buffer concentration lies in a certain interval. Since we use an initial value problem solver to track down a traveling wave, only stable traveling waves are accounted for in Figs. 10 and 11. We expect the full picture to be a reverse *S*—curve as depicted in Fig. 13, with bifurcation occurring when we cross the limit points A_1 and A_2. Because the middle branch in the reverse *S*—curve usually corresponds to the unstable traveling waves, a continuation algorithm[27] has to be employed to trace the full response curve.

When the total buffer concentration is such that there are two stable traveling waves, each of the two stable branches has its own domain of attraction. Initial conditions that are close to one of the stable wave profiles will usually be attracted to it. If we push the total buffer concentration beyond the limit points (say, we start with the wave that belongs to the fast branch and then increase the buffer concentration to the value for which there exists only one stable wave on the slow branch), since now there is only one stable traveling wave, a large change in the wave speed has to take place to settle down into the stable wave profile. Such a discontinuous change is a hallmark of a bifurcation taking place in the system. No similar phenomenon has been observed in the one-variable models.

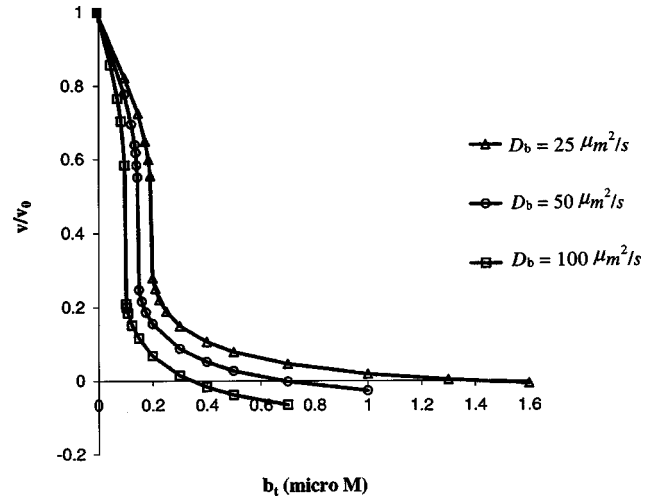

FIG. 11. Wave speed dependencies on the total concentration of a high-affinity buffer ($K=0.1\ \mu$M) at varying buffer diffusion coefficient in the low-excitability mode of the Li–Rinzel model.

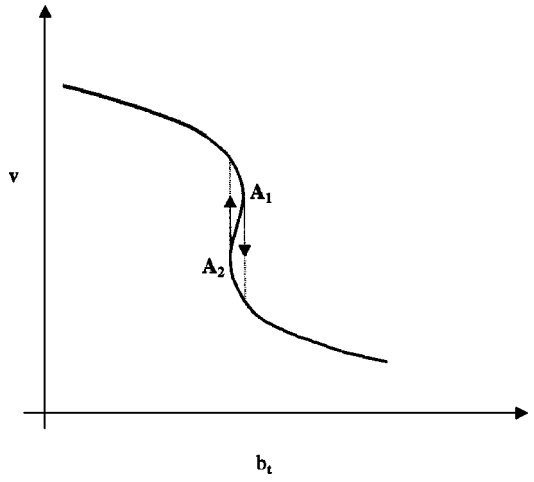

FIG. 13. A full reverse S-curve with the unstable branch A_1A_2.

The experimentally observed fertilization calcium waves[28] are not traveling plane waves, they are rather transient processes initiated by localized spikelike perturbations in a finite domain constrained by a cell membrane. A fluorescent indicator that is used in experiments to visualize calcium dynamics, e.g., fura-2,[29] acts as a high-affinity mobile buffer and, as we saw, can significantly influence the properties of calcium waves. To study the possible effect of the fluorescent indicator on fertilization calcium waves, we have run three-dimensional simulations using realistic geometry, initial, and boundary conditions. In particular, we have simulated fertilization calcium waves in a spherical cell (an egg) using the Li–Rinzel model (3.15) with a physiologically reasonable set of parameters[13] that provides system bistability in the high-excitability mode.

We introduce two types of buffers in our 3D simulations. The immobile low-affinity buffer, with a dissociation constant of 10 μM and a total concentration of 200 μM, represents endogenous buffers, while the mobile high-affinity buffer, with a diffusion coefficient $D_b = 50\ \mu\text{m}^2/\text{s}$ and a dissociation constant $K = 0.24\ \mu\text{M}$, mimics fura-2. A wave is initiated by a calcium spike localized near the cell membrane. The spike is centered at the membrane and has a radius of 5 μm and an amplitude of 30 μM. We run simulations with varying total concentrations of the indicator, b_t. The results show a strong effect of the fluorescent indicator on wave formation. The indicator (the mobile buffer) usually causes a delay in the wave formation and can even prevent a wave if the total concentration of a mobile buffer rises above a certain threshold for the given initial conditions. For our parameter set, this critical concentration is found to be ~ 11 μM.

The simulation results obtained at $b_t = 9.5\ \mu\text{M}$ are presented in Fig. 14. Since in biological experiments one directly measures the fluorescence intensity which correlates well with the bound buffer concentration, it is interesting to compare the dynamics of the bound form of fura-2 with the actual dynamics of free calcium. Figure 14 illustrates a nonlinear relationship between the two dynamics. Thus, care has to be exercised in extracting the calcium dynamics from the experimentally measured fluorescence intensity.[30]

Finally, the calcium waves in the presence of a moderate amount of fura-2 and without it are compared in Fig. 15. The fluorescent indicator strongly interacts with the initiating spike and substantially slows down the wave. Thus, even if the calcium dynamics are correctly extracted from the fluorescent intensity, it can still differ significantly from the actual situation without an indicator.

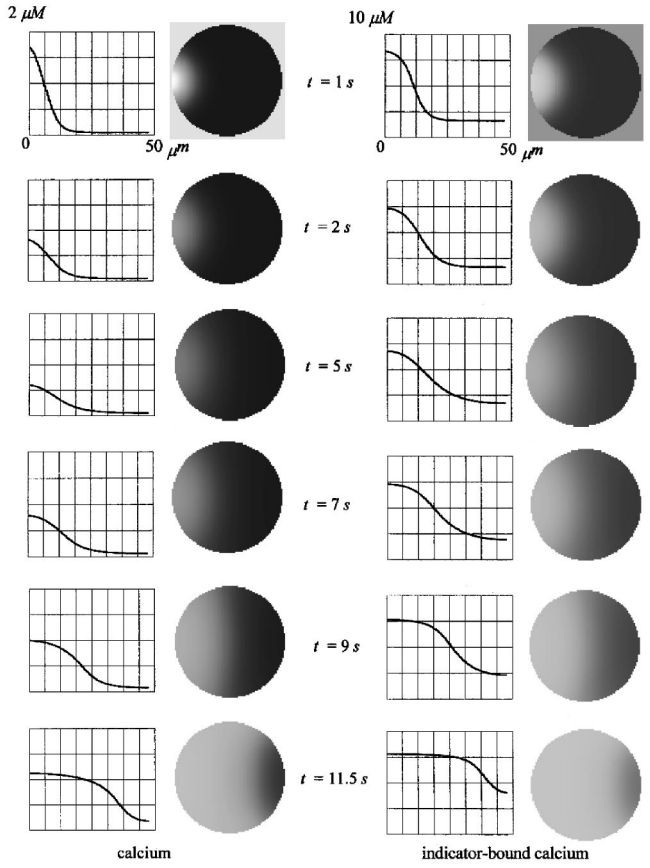

FIG. 14. Calcium wave in the presence of the fluorescent indicator fura-2 ($K = 0.24\ \mu\text{M}$, $D_b = 50\ \mu\text{m}^2/\text{s}$, and $b_t = 9.5\ \mu\text{M}$) (left column), as compared to the dynamics of the indicator-bound calcium that mimics the behavior of the fluorescence intensity (right column). Images of the equatorial slice of an egg are accompanied with a line scan along the cell diameter that coincides with the symmetry axis. Fertilization is initiated at the left pole of the sphere.

IV. CONCLUSION

The Virtual Cell is a computational modeling environment designed to be used by both cell biologists and mathematical biologists. A given cell biological process is defined in terms of which molecules are involved and where they are located within the cell. An intuitive, web-based interface allows the specification of cellular compartment topology; these compartments are then associated with the relevant molecular species and their chemical reaction and transport kinetics. This is sufficient to specify a compartmental model that can then be automatically converted to a system of ordinary differential equations. To implement spatial models, cellular geometry (derived from 2D or 3D experimental or idealized images) is mapped to the previously defined topology and appropriate diffusion coefficients are specified. This then necessitates the solution of partial differential equations. The framework automatically converts the biological mechanisms to a corresponding mathematical system that incorporates mass conservation relationships and pseudo-steady state approximations. The mathematical equations that are generated by the graphical user interface can be viewed and edited, thus facilitating interactions between experimentalists and theoreticians. The Virtual Cell then applies the appropriate numerical solver to perform simulations of intracellular dynamics and analyze simulation results. Several standard solvers including stiff solvers and variable time step solvers are available for the solution of ordinary differential equation. The finite volume method is currently used for PDE problems. Because the simulations produce the same kinds of spatial and temporal records that can be obtained by experiment, the predictions of a model can be analyzed with the same statistical and/or image analysis methods used to

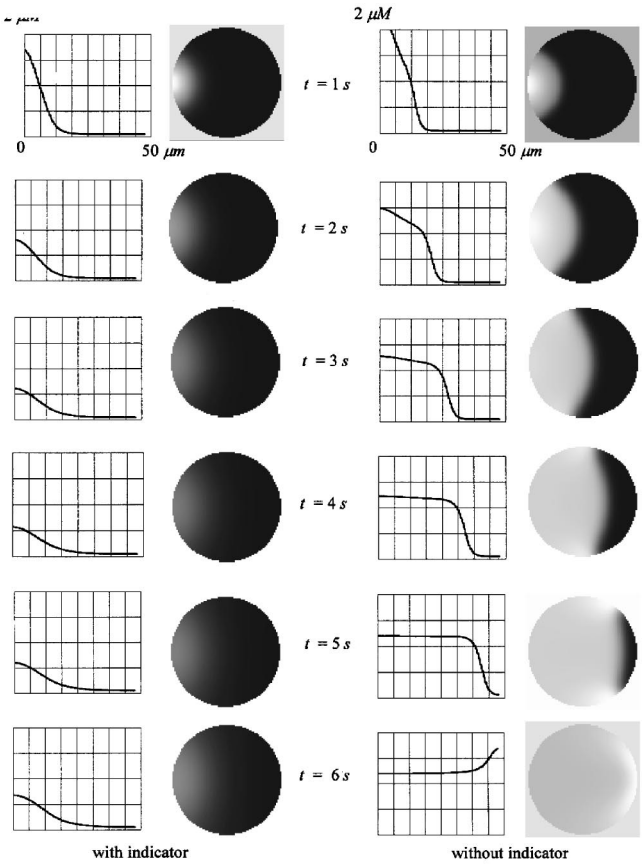

FIG. 15. Simulation of a fertilization calcium wave in the presence of fura-2 ($K=0.24\ \mu$M, $D_b=50\ \mu$m^2/s, and $b_t=9.5\ \mu$M) (left column), and in the absence of a fluorescent indicator (right column). Images of the equatorial slice of an egg are accompanied with a line scan along the cell diameter that coincides with the symmetry axis. Fertilization is initiated at the left pole of the sphere.

analyze experiments. Models, geometries, mathematical systems, and simulation results are stored in a central database that maintains the privacy of user models while providing a mechanism for model sharing. The software is accessible through a web browser via the website of the National Resource for Cell Analysis and Modeling at the U. Conn. Health Center (www.nrcam.uchc.edu).

In this paper, we have described some of the mathematical details that allow the Virtual Cell to be a useful general-purpose tool for the solution of reaction–diffusion equations relevant to biology. We have also provided examples of some applications of the software to problems in calcium dynamics. It is important, however, to note the limitations of the current embodiment of the system and the goals for future improvement. Most important is the improvement of our numerical methods for the solution of PDEs to enable the treatment of realistic large 3D models. These could include stiff spatial solvers, full operator splitting and unstructured grid techniques, as well as finite element-based solvers. Both deterministic and stochastic physical formulations have been implemented, but the latter is still in need of significant development and has not as yet been deployed within the released version of the software. Finally, it is important to note that reaction–diffusion equations alone are not a sufficient physical framework for the solution of all problems in cell biology. Any problem that involves structural dynamics, e.g., cell motility or mitosis, will require new physical formulations and numerics that will need to be integrated with the existing infrastructure for reaction–diffusion. Thus, our efforts to develop the Virtual Cell will continue to offer exciting research challenges as we approach the ultimate goal of enabling mathematical modeling of any cell biological process.

ACKNOWLEDGMENTS

We are pleased to acknowledge support from National Institutes of Health through grants from National Center for Research Resources (Grant Nos. RR13186 and RR10081).

APPENDIX: A PROTOTYPE PROBLEM FOR FLUX CORRECTION

As discussed in Sec. I B, cell geometry can be defined analytically or can be taken directly from an experimental microscope image. To unify both ways of defining geometry, we approximate the cell membrane by a jagged vertical and horizontal boundary as in Fig. 2. In the future, we will treat a smooth cell membrane more accurately, so that in conjunction with other improvements, we can obtain a higher-order method. In what follows, we will show that the method of flux correction on the staircase membrane described in Sec. II B ensures convergence in some norm. We start with a model linear elliptic problem and then extend results to a linear parabolic problem. It is physically clear that the convergence should be also observed in the nonlinear parabolic case because the suggested treatment of membrane fluxes is independent of whether the reaction term is linear or nonlinear.

Case I: the elliptic problem.

Let $f:\mathbf{R}^N\to\mathbf{R}$ be in L^2_{loc} and $g:\mathbf{R}^N\to\mathbf{R}$ be continuous. Given a C^1 domain $\Omega\subset\mathbf{R}^N$ and consider an elliptic problem

$$\nabla^2 u - u = -f, \quad x\in\Omega,$$
$$\left.\frac{\partial u}{\partial n}\right|_{\partial\Omega} = g. \tag{A1}$$

Physically g is the flux per unit surface area of the domain. Next, we replace Ω by another Lipschitz domain $\tilde{\Omega}$, and study

$$\nabla^2 \tilde{u} - \tilde{u} = -f, \quad x\in\tilde{\Omega},$$
$$\left.\frac{\partial \tilde{u}}{\partial n}\right|_{\partial\tilde{\Omega}} = \tilde{g}. \tag{A2}$$

We will prove that u and $\tilde{u}$ are close to one another in some norm, when $\tilde{\Omega}$ is a good staircase approximation to Ω, provided that $\tilde{g}$ is chosen properly. For easy exposition, we assume that $\Omega\in\tilde{\Omega}$ in the proof. We caution that even in the case when $g=1$, we cannot choose $\tilde{g}=1$ because the staircase domain has much larger surface area than that of Ω and consequently the total flux into the domains Ω and $\tilde{\Omega}$ are substantially different.

For all test function $\varphi \in C^\infty(\overline{\Omega})$ [and hence for all test function in $H^1(\Omega)$ by approximation], weak H^1 solution u satisfies

$$\int_\Omega [\nabla u \cdot \nabla_\varphi + u\varphi - f\varphi] = \int_{\partial\Omega} g\varphi, \tag{A3}$$

and a similar equation for $\tilde{u}$.

Since the domain Ω is C^1, recall the standard bounded linear extension operator $E: H^1(\Omega) \to H^1(\mathbf{R}^N)$.[31] Thus there exists a constant $C>0$ such that for all $v \in H^1(\Omega)$, $Ev = v$ in Ω, and

$$\|E_v\|_{H^1(\mathbf{R}^N)} \leqslant C\|v\|_{H^1(\Omega)}. \tag{A4}$$

For simplicity, we will denote Ev by v from now on. We now extend u to a $H^1(\mathbf{R}^N)$ function.

Define a H^1 function $w \equiv \tilde{u} - u$ in $\tilde{\Omega}$. From Eq. (A3) and the corresponding equation for $\tilde{u}$, we obtain

$$\int_{\tilde{\Omega}} [\nabla_w \cdot \varphi + w\varphi] = \int_{\tilde{\Omega}\setminus\Omega} [f\varphi - \nabla u \cdot \nabla\varphi - u\varphi] + \int_{\tilde{\Gamma}} \tilde{g}\varphi - \int_\Gamma g\varphi, \tag{A5}$$

where Γ and $\tilde{\Gamma}$ are part of the boundary as indicated in Fig. 2.

We will take $\varphi = w$ in the above equation. In case of zero boundary flux, i.e., $g = \tilde{g} = 0$, we see that

$$\begin{aligned}
\|w\|^2_{H^1(\tilde{\Omega})} &\leqslant \|f\|_{L^2(\tilde{\Omega}\setminus\Omega)}\|w\|_{H^1(\tilde{\Omega}\setminus\Omega)} + \|u\|_{H^1(\tilde{\Omega}\setminus\Omega)}\|w\|_{H^1(\tilde{\Omega}\setminus\Omega)} \\
&\leqslant \|f\|_{L^2(\tilde{\Omega}\setminus\Omega)}\|w\|_{H^1(\tilde{\Omega})} + \|u\|_{H^1(\tilde{\Omega}\setminus\Omega)}\|w\|_{H^1(\tilde{\Omega})} \\
&\leqslant \tfrac{1}{2}\|w\|^2_{H^1(\tilde{\Omega})} + 2\|f\|_{L^2(\tilde{\Omega}\setminus\Omega)} + 2\|u\|_{H^1(\tilde{\Omega}\setminus\Omega)}.
\end{aligned} \tag{A6}$$

Since $\|f\|_{L^2(\tilde{\Omega}\setminus\Omega)}$ and $\|u\|_{H^1(\tilde{\Omega}\setminus\Omega)}$ go to zero as $\mathrm{meas}(\tilde{\Omega}\setminus\Omega) \to 0$, we have $\tilde{u} \to u$ in $H^1(\Omega)$.

With nonzero boundary flux g and a proper choice of $\tilde{g}$, if we can show that with $\varphi = w$, the difference in the last two terms on the right-hand-side of (A5) is small, then the same argument leads to $\tilde{u} \to u$ in $H^1(\Omega)$. For simplicity, we assume the domain to be two-dimensional although only a slightly more complicated book keeping is required for higher dimensions. Then, according to our approach described in Sec. II B, the corrected flux density $\tilde{g}$ is defined by Eq. (2.8).

Let all the horizontal and vertical segments with the same $\overline{\mathbf{x}}_i$ be denoted by $\tilde{\Gamma}_{i,h}$ and $\tilde{\Gamma}_{i,v}$, respectively. Then, from their definitions, $\int_{\tilde{\Gamma}} \tilde{g} w\, ds = \Sigma_i \int_{\tilde{\Gamma}_{i,h}} g(\overline{\mathbf{x}}_i) w \cos\overline{\theta}_i\, dx + \Sigma_i \int_{\tilde{\Gamma}_{i,v}} g(\overline{\mathbf{x}}_i) w \sin\overline{\theta}_i\, dy$. In addition, $\int_\Gamma g w\, ds = \int_\Gamma g w \times (\cos^2\theta + \sin^2\theta) ds = \int_\Gamma g w \cos\theta\, dx + \int_\Gamma g w \sin\theta\, dy$. We note that w are evaluated at two different locations Γ and $\tilde{\Gamma}$ in the above two equations.

For all $\mathbf{x} \in \tilde{\Gamma}_{i,h}$, let their x-coordinate satisfy $a_i \leqslant x \leqslant b_i$. Thus

$$\begin{aligned}
H &\equiv \left| \int_\Gamma g w \cos\theta\, dx - \Sigma_i \int_{\tilde{\Gamma}_{i,h}} g(\overline{\mathbf{x}}_i) w \cos\overline{\theta}_i dx \right| \\
&\leqslant \Sigma_i \left\{ \left| \int_{a_i}^{b_i} (g\cos\theta - g(\overline{\mathbf{x}}_i)\cos\overline{\theta}_i) w\, dx \right| \right. \\
&\quad \left. + \left| \int_{a_i}^{b_i} g(\overline{\mathbf{x}}_i)\cos\overline{\theta}_i \int (\partial w/\partial y)\, dy \right| \right\}.
\end{aligned}$$

With h small enough, we can assume that $|g\cos\theta - g(\overline{\mathbf{x}}_i)\cos\overline{\theta}_i| \leqslant \epsilon$. Hence, there exist constants $C_i > 0$, $i = 2,3,\ldots$ such that

$$\begin{aligned}
H &\leqslant \epsilon \int_\Gamma |w| + C_2 \int \int_{\tilde{\Omega}\setminus\Omega} \left| \frac{\partial w}{\partial y} \right| dx\, dy \\
&\leqslant \epsilon C_3 \|w\|_{H^1(\Omega)} + C_3 \sqrt{\mathrm{meas}(\tilde{\Omega}\setminus\Omega)}\|w\|_{H^1(\tilde{\Omega})} \\
&\leqslant C_3 \|w\|_{H^1(\tilde{\Omega})} (\epsilon + \sqrt{\mathrm{meas}(\tilde{\Omega}\setminus\Omega)}) \\
&\leqslant 2\epsilon C_3 \|w\|_{H^1(\tilde{\Omega})},
\end{aligned} \tag{A7}$$

after invoking the trace theorem.[31] Inequality (A7) and a similar one for integration over $\tilde{\Gamma}_{i,v}$ lead to

$$\left| \int_{\tilde{\Gamma}} \tilde{g} w - \int_\Gamma g w \right| \leqslant 4 C_3 \epsilon \|w\|_{H^1(\tilde{\Omega})} \leqslant \tfrac{1}{4}\|w\|^2_{H^1(\tilde{\Omega})} + C_4 \epsilon^2,$$

when $\mathrm{meas}(\tilde{\Omega}\setminus\Omega)$ is sufficiently small. Thus, this last term has to be added to the right-hand side of inequality (A6). The same argument allows us to recover $\tilde{u} \to u$ in $H^1(\Omega)$ even when the boundary flux is nonzero.

Case II: the parabolic problem.

Fix any $T>0$. Let $f: \mathbf{R}^N \times [0,T] \to \mathbf{R}$ be in L^2_{loc} and $g: \mathbf{R}^N \times [0,T] \to \mathbf{R}$ be continuous. Again, we have a C^1 domain $\Omega \subset \tilde{\Omega}$, which is a staircase approximation. Let $Q_T \equiv \Omega \times [0,T]$, and $\tilde{Q}_T \equiv \tilde{\Omega} \times [0,T]$. We consider

$$\begin{aligned}
&\nabla^2 u - u - u_t = -f, \quad x \in Q_T, \\
&\left. \frac{\partial u}{\partial n} \right|_{\partial\Omega} = g, \\
&u(x,0) = u_0(x) \ \text{ in } \ \Omega.
\end{aligned} \tag{A8}$$

Similarly,

$$\begin{aligned}
&\nabla^2 \tilde{u} - \tilde{u} - \tilde{u}_t = -f, \quad x \in \tilde{Q}_T, \\
&\left. \frac{\partial \tilde{u}}{\partial n} \right|_{\partial\Omega} = \tilde{g}, \\
&\tilde{u}(x,0) = u_0(x) \ \text{ in } \ \tilde{\Omega}.
\end{aligned} \tag{A9}$$

Here we have assumed that the initial condition u_0 for u and $\tilde{u}$ are the same in Ω, hence we use the same symbols for two different initial conditions. Let $u_0 \in L^2_{\mathrm{loc}}(\mathbf{R}^N)$.

Extend u to $\mathbf{R}^N \times [0,T]$, and define a function $w \equiv \tilde{u} - u$ in $\tilde{Q}_T$. Hence $w(x,0) = 0$ in Ω. We then follow similar ideas in getting Eq. (A5) as in the elliptic case. After we put the test function φ to be w, we have for any $t \in (0,T]$,

$$\frac{1}{2}\int_{\tilde{\Omega}} w^2(\cdot,t) + \int\int_{\tilde{Q}_t} [|\nabla w|^2 + w^2]$$

$$= \frac{1}{2}\int_{\tilde{\Omega}\setminus\Omega} w^2(\cdot,0) + \int_0^t \int_{\tilde{\Omega}\setminus\Omega} \{fw - \nabla_u \cdot \nabla w - uw\}$$

$$+ \int_0^t \left\{ \int_{\tilde{\Gamma}} \tilde{g}w - \int_{\Gamma} gw \right\}. \tag{A10}$$

Similar calculations lead to $\max_{0\leqslant t\leqslant T}\int_{\Omega} w^2(\cdot,t) + \int\int_{Q_T}[|\nabla^2 w|^2 + w^2]$ goes to zero as $\text{meas}(\tilde{\Omega}\setminus\Omega)\to 0$.

[1] P. Mendes, Comput. Applic. Biosci. **9**, 563 (1993).
[2] M. Hines, in *Neural Systems: Analysis and Modeling*, edited by F. Eeckman (Kluwer, Norwell, MA, 1993), pp. 127–136.
[3] J. Bower and D. Beeman, *The Book of GENESIS: Exploring realistic Neural Models with the General Neural Simulation System* (Springer-Verlag, New York, 1994).
[4] P. Grindrod, *The Theory and Applications of Reaction Diffusion Equations. Patterns and Waves* (Oxford University Press, Oxford, 1996).
[5] C. Reder, J. Theor. Biol. **135**, 175 (1988).
[6] J. Schaff *et al.*, Biophys. J. **73**, 1135 (1997).
[7] S. Patankar, *Numerical Heat Transfer and Fluid Flow* (Taylor and Francis, Washington D.C., 1980).
[8] G. Smith, *Numerical Solution of Partial Differential Equations: Finite Difference Methods*, 2nd ed. (Oxford University Press, Oxford, 1978).
[9] J. Thomas, *Numerical Partial Differential Equations: Finite Difference Methods* (Springer-Verlag, New York, 1995).
[10] P. Concus, G. Golub, and D. O'Leary, in *Sparse Matrix Computations*, edited by J. Bunch and D. J. Rose (Academic, New York, 1976).
[11] J. Sneyd, J. Keizer, and M. J. Sanderson, FASEB J. **9**, 1463 (1995).
[12] J. Wagner and J. Keizer, Biophys. J. **67**, 447 (1994).
[13] B. Slepchenko, J. Schaff, and Y. Choi, J. Comput. Phys. **162**, 186 (2000).
[14] N. Yanenko, *The Method of Fractional Steps* (Springer-Verlag, New York, 1971).
[15] J. P. Sørensen and W. E. Stewart, AIChE J. **26**, 98 (1980).
[16] M. J. Berridge, in *Cell to Cell Signalling: From Experiments to Theoretical Models*, edited by A. Goldbeter (Academic, London, 1989).
[17] M. Terasaki *et al.*, Proc. Natl. Acad. Sci. U.S.A. **91**, 7510 (1994).
[18] C. Fink *et al.*, Biophys. J. **79**, 163 (2000).
[19] C. C. Fink *et al.*, J. Cell Biol. **147**, 929 (1999).
[20] Y.-X. Li and J. Rinzel, J. Theor. Biol. **166**, 461 (1994).
[21] N. L. Allbritton, T. Meyer, and L. Stryer, Science **258**, 1812 (1992).
[22] J. Sneyd, Biophys. J. **67**, 4 (1994).
[23] J. Keener and J. Sneyd, *Mathematical Physiology* (Springer-Verlag, New York, 1998).
[24] J. Wagner, Y.-X. Li, J. Pearson, and J. Keizer, Biophys. J. **75**, 2088 (1998).
[25] A. I. Volpert, V. A. Volpert, and V. A. Volpert, *Traveling Wave Solutions of Parabolic Systems* (American Mathematical Society, New York, 1994).
[26] J. Sneyd, P. Dale, and A. Duffy, SIAM (Soc. Ind. Appl. Math.) J. Appl. Math. **58**, 1178 (1998).
[27] H. Keller, *Lectures on Numerical Methods in Bifurcation Problems* (Springer-Verlag, New York, 1986).
[28] L. F. Jaffe, in *Biology of Fertilization*, edited by C. B. Metz and A. Monroy (Academic, Orlando, FL, 1989), Vol. 3.
[29] R. Nuccitelli, *Methods in Cell Biology* (Academic, San Diego, 1994), Vol. 40.
[30] G. Grynkiewicz, M. Poenie, and R. Y. Tsien, J. Biol. Chem. **260**, 3440 (1985).
[31] L. Evans, *Partial Differential Equations, Vol. 19 of Graduate Studies in Mathematics* (American Mathematical Society, New York, 1998).